Magnetic and structural phase diagram of the solid solution $LaCo_xMn_{1-x}O_3$

C. L. Bull,[1,*] H. Y. Playford,[1] K. S. Knight,[1,2,3] G. B. G. Stenning,[1] and M. G. Tucker[1,4,†]
[1]*STFC ISIS Facility, Rutherford Appleton Laboratory, Didcot OX11 0QX, United Kingdom*
[2]*Department of Earth Sciences, The Natural History Museum, Cromwell Road, London SW7 5BD, United Kingdom*
[3]*Department of Earth Sciences, University College London, Gower Street, London WC1E 6BT, United Kingdom*
[4]*Diamond Light Source, Ltd., Harwell Oxford, Didcot OX11 0DE, United Kingdom*
(Received 22 February 2016; revised manuscript received 3 May 2016; published 5 July 2016)

We present a structural and magnetic phase diagram of the solid solution $LaCo_xMn_{1-x}O_3$. We show by neutron diffraction that the monoclinic structure previously observed for the elpasolite form La_2CoMnO_6 ($LaCo_{0.5}Mn_{0.5}O_3$) is also observed for another member of the solid solution $x = 0.35$. We also present the transition temperatures for the orthorhombic/monoclinic structures of the series to the rhombohedral structure and determine the expected transition temperatures from rhombohedral to cubic symmetry. We present the magnetic structures as determined by neutron diffraction for materials with lower cobalt content and provide evidence, including ac and dc susceptibility measurements, for the possible glassy nature of the magnetism in the cobalt-rich materials in the series. Based on high-resolution neutron diffraction, we also suggest that there is a limit to the $LaCo_xMn_{1-x}O_3$ solid solution at $x = 0.85$. Finally we present a possible, previously unreported, low-temperature monoclinic structure for the sample $LaCo_{0.75}Mn_{0.25}O_3$.

DOI: 10.1103/PhysRevB.94.014102

I. INTRODUCTION

Perovskites with the general formula ABO_3 (where A is often a lanthanide and B commonly a transition metal) are an important and widely studied class of materials, characterized by subtle structural distortions from the cubic aristotype (characterized by space group $Pm\bar{3}m$). The ideal perovskite structure consists of a corner-shared network of BO_6 octahedra with the larger A cations sitting in interstitial sites coordinated by 12 O atoms. The enormous variety of physical and chemical properties that the perovskite family displays arises from the fact that the A and B cations can be selected from a large proportion of the periodic table.

Double perovskites (elpasolite) represent a variant of the perovskite structure with the general formula $A_2BB'X_6$ in which the prime indicates the possibility of different cations. In general, the B-site cations determine the physical properties of the double perovskites, and three B-cation sublattice types are recognized, random, rock-salt, and layered, with the latter two demonstrating an ordered arrangement of the resulting BX_6 octahedra. B-site ordering in double perovskites typically occurs when there is a significant charge and/or size difference between the B and B' cations.

The solid solution $LaCo_xMn_{1-x}O_3$ has been the subject of a large body of work focused on understanding its complex structure-property relationships. It is closely related to the A-site doped manganites, which famously exhibit colossal magnetoresistance [1], and itself displays a wealth of interesting magnetic and electronic properties which change as a function of x. Furthermore, mixed-metal perovskite oxides are increasingly of interest for catalytic applications [2–4]. For example, it has been shown that low-level doping of $LaCoO_3$ with Mn forms an effective catalyst for the oxidation of particulate matter in vehicle exhaust [5].

The $x = 1$ end member, $LaCoO_3$, undergoes some well characterized temperature-driven electronic transitions. At low temperature (<50 K), $LaCoO_3$ is a nonmagnetic insulator with the trivalent cobalt in the low-spin (LS) state configuration $t_{2g}^6e_g^0$. At ~100 K the material becomes paramagnetic and with increasing temperature the high-spin (HS) $t_{2g}^4e_g^2$ configuration is populated. Above 648 K charge transfer between spin states occurs and disproportionation into Co^{2+} and Co^{4+} species is observed [6]. Structurally, $LaCoO_3$ is rhombohedral, space group $R\bar{3}c$ ($a^-a^-a^-$ in Glazer notation, representing three antiphase tilts around the cubic a, b, and c axes) [7,8]. In contrast, at the other end of the series $LaMnO_3$ ($x = 0$) is an antiferromagnet (Néel temperature 140 K), an insulator, and crystallizes in an orthorhombic structure (space group $Pbnm$) [9]. This hetto-type structure results from antiphase rotations of the MnO_6 octahedra about the [100] cubic/[010] cubic directions and in-phase rotations around the [001] cubic direction and can be described by the $a^-a^-c^+$ tilt system in Glazer notation [8].

For members of the solid solution rich in cobalt ($x > 0.6$), the rhombohedral structure dominates, whereas for $x < 0.6$ the orthorhombic structure is found (for $x = 0.6$ a biphasic mixture is observed) [10]. The structure of the material with $x = 0.5$ has been a matter of some debate over the years and has been reported as cubic [11], orthorhombic [12], or even biphasic in nature [13]. However, high-resolution neutron diffraction data show that the sample crystallizes in the monoclinic space group $P2_1/n$ (tilt system $a^-a^-c^+$), which is a maximal nonisomorphic subgroup of the orthorhombic $Pbnm$. In the monoclinic structure, the manganese and cobalt cations order at the 90% level on the $2b$ and $2c$ sites, respectively [14].

For the $LaCo_xMn_{1-x}O_3$ solid solution there have been numerous magnetic property studies, and in 1961 Goodenough *et al.* [13] suggested that across the series the cobalt ions were in the diamagnetic low-spin state Co^{3+} and hence only

*craig.bull@stfc.ac.uk
†Present address: Spallation Neutron Source, One Bethel Valley Road, MS-6475, Oak Ridge, Tennessee 37830, USA.

the ferromagnetic Mn^{3+}–O^{2-}–Mn^{3+} and Mn^{3+}–O^{2-}–Mn^{4+} interactions contributed to the magnetic properties. However, further magnetic and electrical characterization studies by Jonker showed that there is also a contribution from Mn^{4+}–O^{2-}–Co^{2+}, Mn^{3+}–O^{2-}–Mn^{3+}, and Mn^{3+}–O^{2-}–Mn^{4+} superexchange interactions through the anions [15]. Work by Troyanchuk *et al.* [16] found that the magnetic properties of $LaCo_xMn_{1-x}O_3$ could be explained on the basis of positive Mn^{3+}–Mn^{4+}, Mn^{3+}–Mn^{3+}, Mn^{4+}–Co^{2+} and negative Mn^{4+}–Mn^{4+}, Co^{2+}–Co^{2+}, Co^{2+}–Mn^{3+} superexchange interactions combined with Mn^{4+} and Co^{2+} cation ordering. In a more recent study combining both magnetic and transport properties, it was shown that for the orthorhombic manganese-rich region, cobalt enters as Co^{2+} and induces a mixed Mn^{3+}/Mn^{4+} valence state in the manganese. For $x \approx 0.4$ the majority of the ions are Co^{3+} and Mn^{3+}, and in the rhombohedral cobalt-rich region the manganese is present preferentially in the Mn^{4+} state, inducing electronlike carriers in the Co-O subarray [10]. In contrast with this, Sikora *et al.* [17] found from x-ray absorption spectroscopy that the valence of both cations increases almost linearly with x, and furthermore, that they are mixed valent across the entire solid solution.

The bulk magnetization behavior of these materials reflects the complexity of the underlying interactions. For $0.4 \leqslant x \leqslant 0.9$, Troyanchuk *et al.* [16] proposed a mixture of cationically ordered ferromagnetic and disordered spin-glass regions, and noted that samples quenched from high temperature had an increased fraction of spin-glass-like domains. Autret *et al.* [10] observed a crossover from predominantly ferromagnetic interactions at low Co content to predominantly antiferromagnetic interactions at $x = 1$. For $x = 0.4$, a two-step transition to a bulk ferromagnetic phase has been observed and attributed to the presence of ferromagnetic clusters forming at the higher transition temperature and coalescing to produce long-range order (observable by neutron diffraction) at the lower. Whether these clusters result from intrinsic chemical inhomogeneity or from the presence of distinct cation ordered and disordered regions is the subject of some debate [10,18]. For $x = 0.5$, two ferromagnetic phases have been reported: one with a higher T_C ($\sim$225 K), which contains exclusively Co^{2+} and Mn^{4+} and exhibits extensive cation ordering, and a second with a lower T_C ($\sim$150 K), which contains a disordered arrangement of mixed valent cations [19,20]. The coexistence of these phases is almost unavoidable, though the fraction of each can be controlled by the preparation method followed [19,21]. It is therefore perhaps unsurprising that a range of magnetic ground states has been proposed, from long-range ferromagnetic order [22] to cluster-glass models [23], and even superparamagnetism [24]. For $x = 0.8$, a similar, though less pronounced, nonuniform magnetic behavior was observed and was attributed to the existence of small ferromagnetic clusters in a disordered matrix [10]. Furthermore, a peak in the magnetic susceptibility at 25 K was attributed to a spin-glass transition.

We have synthesized and studied materials in the $LaCo_xMn_{1-x}O_3$ series (with $x = 0.2, 0.35, 0.5, 0.75$, and 0.9). Based upon these studies we present a structural phase diagram for this solid solution. We show that crystallographic ordering of the Co/Mn ions occurs at room temperature not only for $x = 0.5$, but also for $x = 0.35$, and we suggest that the sample with $x = 0.75$ undergoes a rhombohedral-to-monoclinic phase transition at $\sim$100 K. We have also determined temperatures for the high-temperature rhombohedral-to-cubic transition for each sample studied. We have used neutron diffraction and magnetometry to analyze the magnetic structure of all the materials in the series and present evidence for a glassy ferromagnetic behavior in the cobalt-rich samples.

II. EXPERIMENTAL

A. Synthesis and x-ray characterization

Polycrystalline samples of $LaCo_xMn_{1-x}O_3$ were prepared by a modified nitrate decomposition route. Appropriate mixtures of hydrated metal nitrate salts were dissolved in the minimum amount of hot water in an alumina crucible, and decomposition was achieved first by heating to dryness on a hotplate and then by a slow heating to 870 K in a tube furnace in air. Samples were subsequently annealed at 1270 K for 12 h and were cooled at a rate of $\sim$2 K min^{-1} again in an air atmosphere. The degree of phase purity of the perovskite was determined by x-ray diffraction (XRD) with a Rigaku Miniflex x-ray diffractometer using Cu $K_{\alpha 1,2}$ radiation. High-temperature XRD was carried out on a Rigaku SmartLab diffractometer fitted with a germanium (220) monochromator. An Anton Paar HTK high-temperature stage was used to collect diffraction patterns in the temperature range 293–1200 K.

B. Variable-temperature neutron diffraction

Ambient- and low-temperature time-of-flight neutron diffraction measurements were carried out on the Polaris and High Resolution Powder Diffractometer (HRPD) instruments at ISIS, the UK's spallation neutron source at the Rutherford Appleton Laboratory. Initially, room-temperature and 50 K diffraction patterns were collected from all samples using the medium-resolution, high-flux Polaris diffractometer [equipped with an Abingdon Scientific (AS) "Orange" cryostat for the low-temperature measurements]. Subsequent detailed characterization of the cobalt-rich end of the series was carried out on the high-resolution HRPD instrument at temperatures in the range 4.2–300 K again using an AS "Orange" cryostat.

C. Magnetic characterization

The dc magnetization measurements were carried out using a Quantum Designs MPMS-XL7 (SQUID) magnetometer. A finely ground powder sample of known mass was placed into a gelatine capsule and mounted into a straw before being introduced into the instrument at 300 K. Measurements of the dc magnetization were made as a function of temperature (1.8–300 K) in an applied field of 100 Oe and in both field-cooled (FC) and zero-field-cooled (ZFC) conditions. Hysteresis loops were also measured ($\pm$5 T) as a function of temperature in the range 10–250 K.

The ac magnetic susceptibility was measured using a Quantum Designs PPMS-9 equipped with an ac measurement system (ACMS). The powdered sample was pressed into a

pellet and annealed at 1100 °C for ∼8 hours prior to loading into a straw as described above. Magnetization measurements at various temperatures (2–300 K) were carried out in zero-field-cooled upon warming (ZFCW) conditions, with dc bias fields between 0 and 1000 Oe, an ac field magnitude of 10 Oe, and at a range of frequencies between 250 and 10 000 Hz.

III. RESULTS AND DISCUSSION

A. X-ray characterization

The samples were shown by Rietveld refinement to be, on the whole, single phase, except for a small contaminant of La_2O_3 (∼2–3wt %). X-ray diffraction confirmed the crystallographic symmetry (within instrument and technique resolution) to be orthorhombic ($Pbnm$) for the $x = 0.2$ and 0.35 samples, monoclinic ($P2_1/n$) for the $x = 0.5$ sample, and rhombohedral ($R\bar{3}c$) for the 0.75 and 0.9 samples. Despite extensive efforts we were unable to prepare a phase pure sample with the composition of $x = 0.6$ and can confirm previous reports that an ≃50 : 50 mixture of rhombohedral and orthorhombic phases were present [10]. The relative proportion of Co and Mn in each sample was confirmed to lie within error of the intended stoichiometry using x-ray fluorescence (XRF).

B. X-ray characterization at high temperature

The high-temperature structural behavior of all samples in the series has been studied using XRD. Changes are observed in the region of the 112, 020, and 200 reflections at around ∼2.75 Å in the orthorhombic/monoclinic phases ($x = 0.2$, 0.35, and 0.5) with increasing temperature, as previously reported for $x = 0.33$ [25]. Indexing of the high-temperature diffraction pattern above 573 K shows that the reflections are consistent with rhombohedral symmetry (indexed with the $R\bar{3}c$ space group in the rhombohedral metric in the case of $x = 0.2$ and 0.35 and $R\bar{3}$ for $x = 0.5$). Shown in the lower-right panel of Fig. 1 is the evolution of the 211 and 101 reflections for the rhombohedral $LaCo_{0.9}Mn_{0.1}O_3$, which

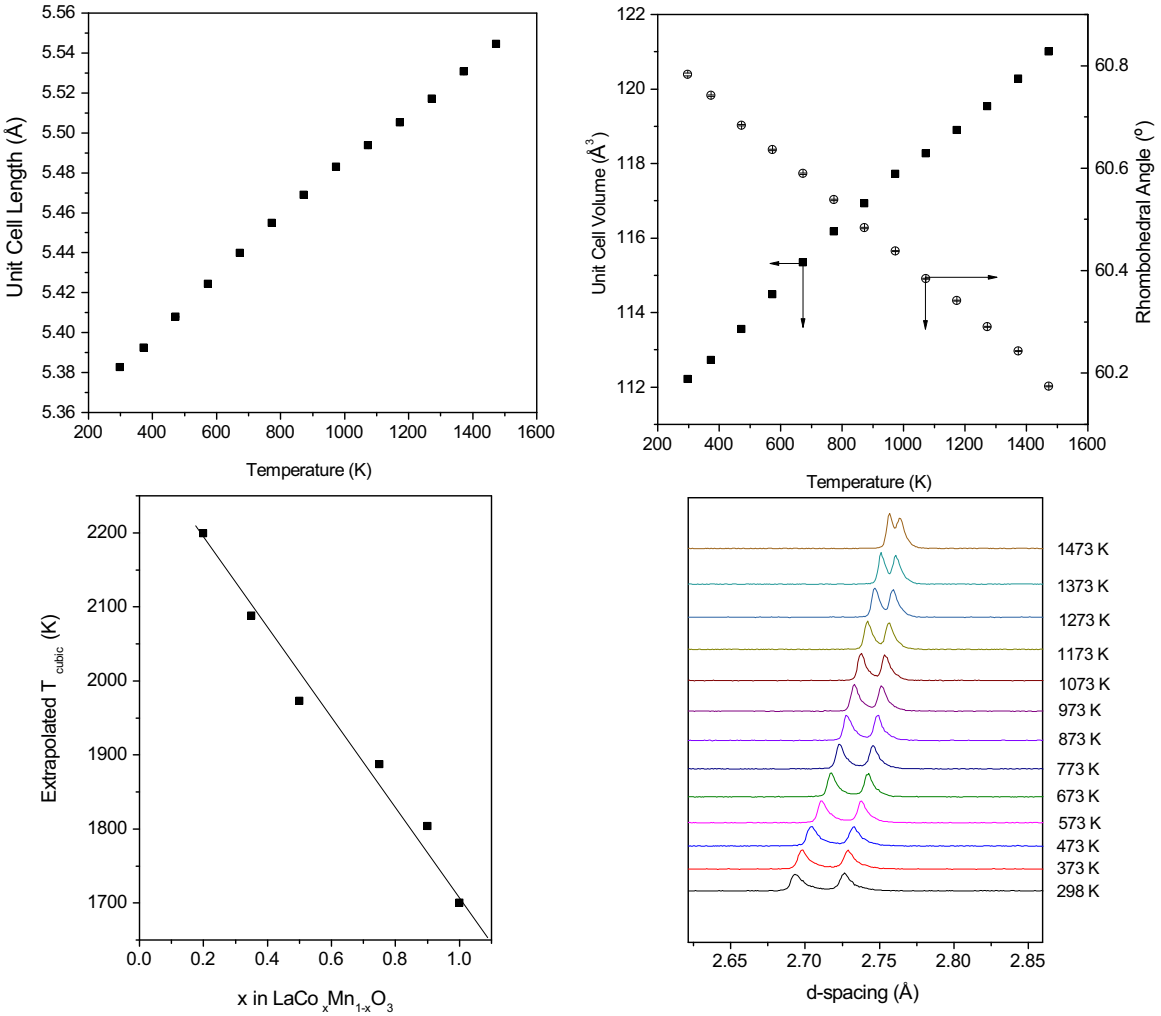

FIG. 1. Upper: The variation of determined unit-cell length, volume, and rhombohedral cell angle with temperature for the $x = 0.9$ sample. Lower left: The extrapolated transition temperature from the rhombohedral symmetry to cubic symmetry as a function of x. Lower right: The changes upon heating in the x-ray diffraction pattern of the rhombohedral sample $LaCo_{0.9}Mn_{0.1}O_3$ are shown in the lower-right panel. The 211 and 101 reflections are shown at ∼2.69 and 2.72 Å, respectively, and are shown to shift to higher d spacing with increasing temperature, and the spacing between the reflections is decreasing with increasing temperature.

move to higher d spacing as a result of thermal expansion of the unit cell and whose separation decreases with increasing temperature, as a result of the decrease of the rhombohedral unit-cell angle. Diffraction patterns measured at 473 K show that there is coexistence of the orthorhombic and rhombohedral phases, as would be expected given the first-order nature of the structural transition [26]. The refined lattice parameters, unit-cell volumes, and rhombohedral unit-cell angles are shown in the upper panels of Fig. 1. Similar behavior has been observed for all of the samples in the series which at ambient conditions are orthorhombic or monoclinic in that they transform to rhombohedral upon warming. The samples in the series which are rhombohedral at room temperature show no phase transitions in the temperature region measured using XRD; however, they do show the same trend in that the splitting of the 211 and 101 reflections decreases with increasing temperature. (The determined unit-cell parameters for $x = 0.9$ are shown in Fig. 1.) Assuming a continued linear behavior of the rhombohedral α angle, it is possible to extrapolate the temperature at which it would become 60°. With an α angle of 60° in the rhombohedral symmetry, it is assumed that the crystallographic symmetry would be transformed to the cubic $Pm\bar{3}m$ via a second-order phase transition, as has been shown previously for other systems such as $LaAlO_3$ and $PrAlO_3$ [27,28]. Figure 1 also shows the variation with x of the temperature at which the rhombohedral angle extrapolates to 60 deg. It is clear that with increasing cobalt content the temperature at which the system becomes metrically cubic decreases. Recently, Orayech *et al.* proposed to have observed pseudocubic symmetry ($Fm\bar{3}m$) in La_2CoMnO_6 at 1545 K (however, that study may have been resolution limited) [22]. Also plotted is the extrapolated temperature at which $LaCoO_3$ is expected to become cubic based upon the work of Thornton *et al.* [7]. However, this is in contrast to the work recently published by Kobayashi *et al.* [29], who suggest a pseudocubic transition at 1610 K (however, it may be that their result is again resolution limited).

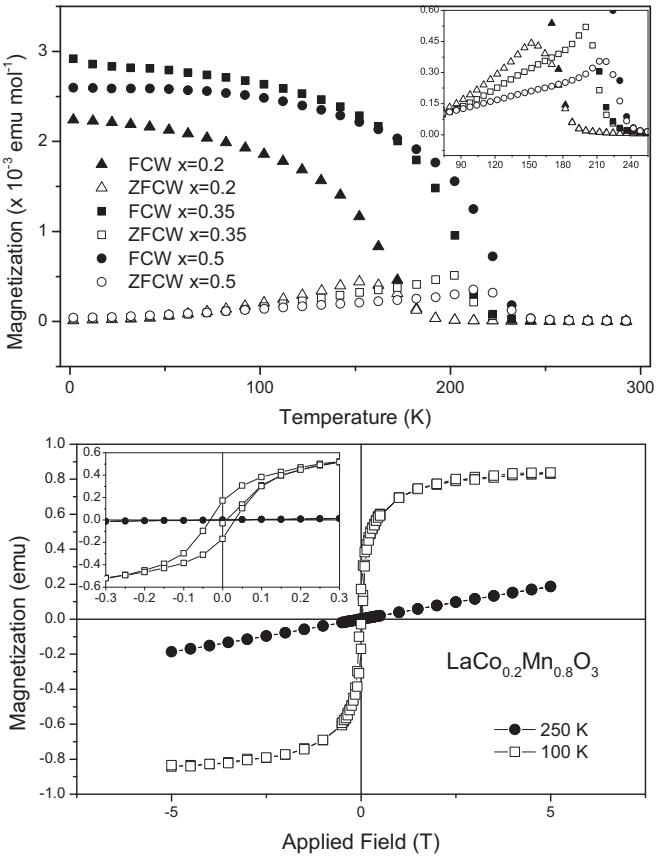

FIG. 2. Upper: Magnetization of $LaCo_xMn_{1-x}O_3$ (for $x = 0.2$, 0.35, and 0.5) as a function of temperature, under both zero-field-cooled warming (ZFCW) and field-cooled warming (FCW) conditions. Insert shows in detail the ZFCW behavior close to the determined Curie temperature. Lower: Typical magnetization versus applied field loops at temperatures above and below T_C for compositions $x = 0.2$, 0.35, and 0.5. No hysteresis is seen above T_C but below, an open loop consistent with ferromagnetic ordering is seen. Insert shows the data close to zero applied field.

C. Magnetic characterization

Bulk dc magnetization measurements have been performed for each of the samples in the series and the results are shown in Figs. 2 and 3. For $x = 0.2$, 0.35, and 0.5 (Fig. 2), the ZFCW and FCW magnetization curves are consistent with the onset of long-range magnetic ordering. We see no evidence for the two-step transition previously reported for $x = 0.4$ and 0.5 [10,18,21,24]. Above T_C the materials obey the Curie-Weiss law, and the fitting to the linear region of an inverse susceptibility versus temperature plot allows the determination of an effective paramagnetic moment, μ_{eff} (Table I). The values of μ_{eff} are larger than the theoretical spin-only moments (even if both cations are assumed to be in a high-spin configuration) and can be explained if the $3d$ orbital contribution to the magnetic moment of Co^{2+} is not fully quenched. This is consistent with our previous report on the $x = 0.33$ composition ($\mu_{\text{eff}} = 5.33\mu_B$/f.u.) [25], and with the findings of Burnus *et al.* [20] for $x = 0.5$. The Weiss constants θ_W, obtained from the x intercepts of the linear fits, are also shown in Table I. The positive values indicate that the magnetic interactions in the materials are predominantly ferromagnetic, and their similarity to T_C for $x \leqslant 0.5$ suggest that these systems are not frustrated. Hysteresis loops (M versus H) are also shown in Fig. 2 and are again consistent with the presence of ferromagnetic order at temperatures below T_C. The hysteresis loop at 100 K reveals an apparent saturation magnetization of 2 μ_B per formula unit, which agrees reasonably well with the value obtained from Rietveld refinement of neutron diffraction data collected at 50 K (see Sec. III D) but is much smaller than the paramagnetic μ_{eff}. This observation suggests that the ferromagnetic ordering is incomplete, perhaps because of the competing interactions and the inherent disorder of the system.

Significantly different magnetic behavior is observed for the samples with $x = 0.75$ and 0.9, as shown in Fig. 3. In general, the response of these samples is much weaker than for the lower-Co-content materials, and furthermore, the ZFCW curves show two distinct features, one at $\sim T_C$ and a second at ~25–30 K. The hysteresis loops measured below 145 K are reminiscent of those for a ferromagnetic material but do not approach saturation, even at high field. At 145 K no hysteresis is seen and little change is observed on further warming. The values of μ_{eff} for these materials are significantly lower than

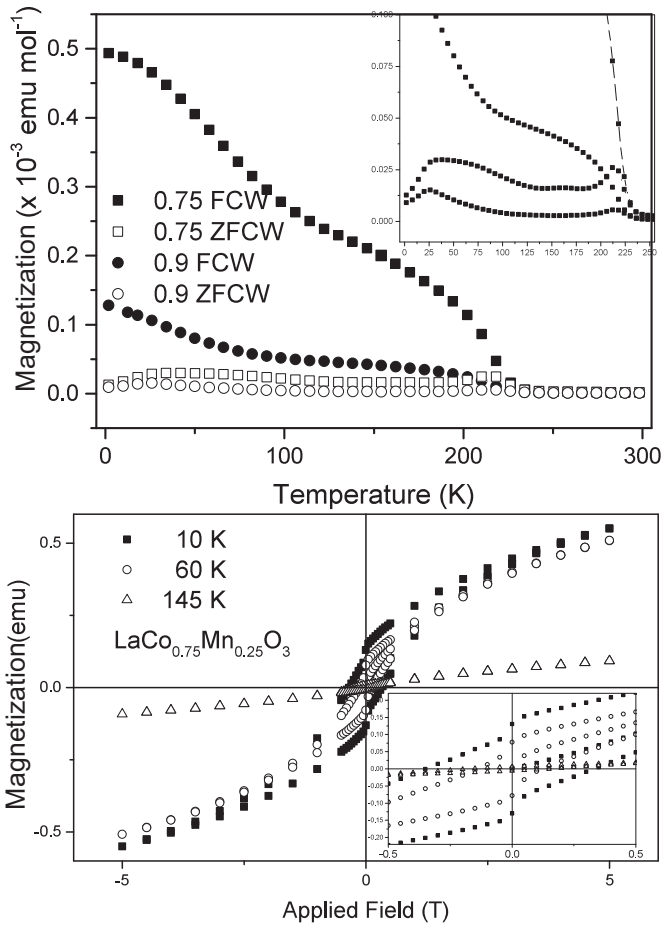

FIG. 3. Upper: Magnetization of $LaCo_xMn_{1-x}O_3$ (for $x = 0.75$, 0.9) as a function of temperature, under both zero-field-cooled warming (ZFCW) and field-cooled warming (FCW) conditions. Insert shows in detail the unusual behavior below 250 K. Lower: Magnetization versus applied field loops for $x = 0.75$ at temperatures above and below the observed features ZFCW data. No hysteresis is seen above 145 K, and below this temperature the curves resemble those expected for a ferromagnetic material but do not approach saturation, even at $H = 5.0$ T.

for the $x \leqslant 0.5$ samples and are consistent with a combination of Mn^{4+} and mixed-valent Co in an intermediate spin (IS) state. (Calculated spin-only moments are 3.34 and 3.01 μ_B for $x = 0.75$ and 0.9, respectively.) There is, of course, much controversy surrounding the assignment of an IS state in $LaCoO_3$ [7,30,31], and given the complexity of the cation distribution and magnetic interactions in $LaCo_xMn_{1-x}O_3$, it is not possible to unambiguously assign oxidation or spin states. The observed moments could also be explained by a mixture of HS and LS states for either or both cations. The values of θ_W for these samples are rather smaller than T_C, which may suggest some degree of frustration is present in these materials. Further discussion of the unusual magnetic behavior of the $x = 0.75$ and 0.9 samples is given in Sec. III D 2.

TABLE I. Magnetic parameters for $LaCo_xMn_{1-x}O_3$.

Sample	T_C (K)[a]	$\mu_{eff}(\mu_B)$	θ_W (K)	Ordered moment (μ_B)[b]
$x = 0.2$	177	4.99	186.36	2.81(1)
$x = 0.35$	208	5.77	216.34	3.01(2)
$x = 0.5$	228	5.33	230.38	3.14(1)
$x = 0.75$	222	3.74	185.67	
$x = 0.9$	224	2.91	143.57	

[a]Defined as a minimum in the first derivative of $\chi(T)$.
[b]Determined from Rietveld refinement against Polaris data collected at 50 K.

D. Neutron diffraction

1. Ambient temperature

Medium-resolution neutron diffraction measurements were performed on the Polaris instrument at room temperature. The focused and absorption-corrected data from all five of Polaris' detector banks were subsequently analyzed using Rietveld refinement, the results of which are shown in Table II. During the refinements the occupancy of the mixed transition-metal sites were constrained to unity but the ratios allowed to refine. We found no evidence for oxygen nonstoichiometry. (O-site occupancies did not change significantly from unity during trial refinements and were subsequently fixed at this value.) The material with $x = 0.2$ was shown to be orthorhombic with space group $Pbnm$, in agreement with previous reports and with x-ray diffraction. In this structure both transition-metal (TM) ions are statistically distributed over a single crystallographic site, and therefore the obtained TM-O distances represent an average value which cannot provide information on the occurrence of (or degree of) charge ordering, or the assignment of possible oxidation states. Of particular interest is the refinement of the sample with the composition $LaCo_{0.35}Mn_{0.65}O_3$. In this case, the $Pbnm$ structure proved unsatisfactory and the data were in fact best fit with a monoclinic structure, space group $P2_1/n$, which has previously been reported only for the sample with $x = 0.5$ [14]. The improvement in goodness-of-fit parameters is detailed in Table II, and the fit itself is shown in Fig. 4. This monoclinic structure provides two distinct sites for the transition-metal ions, and refining the site occupancies on the $2c$ and $2d$ Wyckoff sites reveals a high degree of order and hence different TM-O distances for each cation can be determined. For the samples with composition $x = 0.75$ and 0.9 the symmetry was found to be rhombohedral with the space group $R\bar{3}c$, which again does not allow any transition-metal site ordering and only provides an average TM-O distance.

The reduced lattice parameters for the $LaCo_xMn_{1-x}O_3$ series, as determined from medium-resolution neutron diffraction data, are shown in Fig. 5, along with those reported by Autret *et al.* [10]. Interestingly, we do not observe a pseudocubic lattice (i.e., $a_{pc} \simeq b_{pc} \simeq c_{pc}$) for $x = 0.2$ in the $Pbnm$ space group and instead found that for $x \leqslant 0.5$ the reduced lattice parameters changed only slightly, with $a_{pc} \gg c_{pc} > b_{pc}$ in all cases. The rhombohedral lattice parameter reduces with x, in good agreement with previous reports. The average bond distances show a gradual change from that determined for $LaMnO_3$ to $LaCoO_3$ with increasing cobalt content, as shown in Fig. 6 and detailed in Table II.

For the $x = 0.75$ and 0.9 composition samples, high-resolution neutron powder diffraction data were measured on the HRPD instrument. Data from the 90° bank of detectors

TABLE II. Structural parameters for $LaCo_xMn_{1-x}O_3$ as determined by Rietveld refinement against Polaris data. Parameters for both orthorhombic and monoclinic fits are shown for the sample with $x = 0.35$.

		$x = 0.2$	$x = 0.35$	$x = 0.35$	$x = 0.5$	$x = 0.75$	$x = 0.9$
	Space group	$Pbnm$	$Pbnm$	$P2_1/n$	$P2_1/n$	$R\bar{3}c$	$R\bar{3}c$
	a (Å)	5.5297(1)	5.5258(2)	5.5259(1)	5.52464(9)	5.4071(2)	5.3846(1)
	b (Å)	5.4884(1)	5.4844(2)	5.4840(1)	5.48302(9)	$= a$	$= a$
	c (Å)	7.7774(2)	7.7714(2)	7.7709(1)	7.7717(1)	$= a$	$= a$
	α (°)	90	90	90	90	60.828(1)	60.801(1)
	β (°)	90	90	89.930(3)	89.898(3)	$= \alpha$	$= \alpha$
	γ (°)	90	90	90	90	$= \alpha$	$= \alpha$
	wR_p (%)	2.09	3.03	2.00	2.09	2.87	3.67
	R_p (%)	2.44	3.01	2.16	2.67	3.45	5.23
La	Wyckoff site	4*c*	4*c*	4*e*	4*e*	2*a*	2*a*
	x	0.9947(2)	0.9916(2)	0.0041(1)	0.0057(1)	0.25	0.25
	y	0.0204(1)	0.0212(1)	0.02096(8)	0.02160(9)	0.25	0.25
	z	0.25	0.25	0.2485(2)	0.2438(1)	0.25	0.25
	U_{iso} (Å^2)	0.00775(8)	0.0069(1)	0.00608(7)	0.00400(7)	0.00578(8)	0.00456(8)
	S.O.F.	1	1	1	1	1	1
Co/Mn(1)	Wyckoff site	4*b*	4*b*	2*c*	2*c*	2*b*	2*b*
	x	0.5	0.5	0	0	0	0
	y	0	0	0.5	0.5	0	0
	z	0	0	0	0	0	0
	U_{iso} (Å^2)	0.0024(1)	0.0003(3)	0.001(2)	0.005	0.005	0.005
	S.O.F (Co)	0.213(1)	0.350(2)	0.690(2)	0.881(2)	0.760(1)	0.920(1)
	Co/Mn–O1 (Å)	2 × 1.97817(3)	2 × 1.9774(2)	2 × 2.0247(14)	2 × 2.0371(9)	6 × 1.94496(7)	6 × 1.93485(6)
	Co/Mn–O2 (Å)	2 × 1.97817(3)	2 × 1.9774(2)	2 × 2.0238(15)	2 × 2.0360(9)		
		2 × 1.97654(2)	2 × 1.9781(7)				
	Co/Mn–O3 (Å)			2 × 2.033(2)	2 × 2.0491(9)		
Co/Mn(2)	Wyckoff site			2*d*	2*d*		
	x			0.5	0.5		
	y			0.0	0.0		
	z			0.0	0.0		
	U_{iso} (Å^2)			0.0032(3)	0.005		
	S.O.F (Co)			0	0.119(2)		
	Co/Mn–O1 (Å)			2 × 1.9259(14)	2 × 1.9207(9)		
	Co/Mn–O2 (Å)			2 × 1.9225(15)	2 × 1.9116(9)		
	Co/Mn–O3 (Å)			2 × 1.920(2)	2 × 1.9030(9)		
O1	Wyckoff site	4*c*	4*c*	4*e*	4*e*	6*e*	6*e*
	x	0.0656(1)	0.0664(2)	0.2836(3)	0.2879(2)	–0.19760(4)	–0.19962(4)
	y	0.4948(2)	0.4950(2)	0.2712(3)	0.2732(2)	0.69760(4)	0.69962(4)
	z	0.25	0.25	0.0335(3)	0.0347(2)	0.25	0.25
	U_{iso} (Å^2)	0.0087(2)	0.0077(2)	0.0087(4)	0.0059(2)	0.00817(6)	0.00755(7)
	S.O.F.	1	1	1	1	1	1
O2	Wyckoff site	8*d*	8*d*	4*e*	4*e*		
	x	0.7285(1)	0.7283(1)	0.2631(2)	0.2611(1)		
	y	0.2724(1)	0.2712(1)	0.2765(4)	0.2775(2)		
	z	0.03511(7)	0.03751(8)	0.4633(2)	0.4621(2)		
	U_{iso} (Å^2)	0.0106(1)	0.0088(1)				
	S.O.F.	1	1	1	1		
O3	Wyckoff site			4*e*	4*e*		
	x			0.5652(1)	0.5650(1)		
	y			–0.0062(1)	–0.0053(1)		
	z			0.2425(3)	0.2404(1)		
	U_{iso} (Å^2)			0.0082(2)	0.0073(1)		
	S.O.F.			1	1		

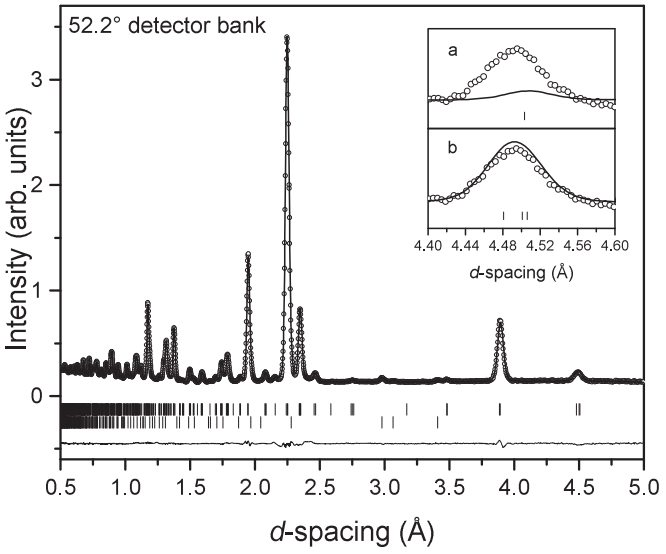

FIG. 4. Result of Rietveld refinement of the $x = 0.35$ sample using the monoclinic $P2_1/n$ structure. Inset (a) shows the poor fit of the orthorhombic model to the data in the region of the 101 reflection, and (b) the significant improvement on allowing the 101 and $10\bar{1}$ to split via the monoclinic β angle being non-90 deg, but also the presence of the 011 reflection, which is a systematic absence in space group *Pbnm*.

were exactly comparable to those measured on Polaris at room temperature. For the $x = 0.9$ composition, data from the 168° backscattering detector bank revealed shoulders on each of the reflections. The best fit to these data was obtained with a

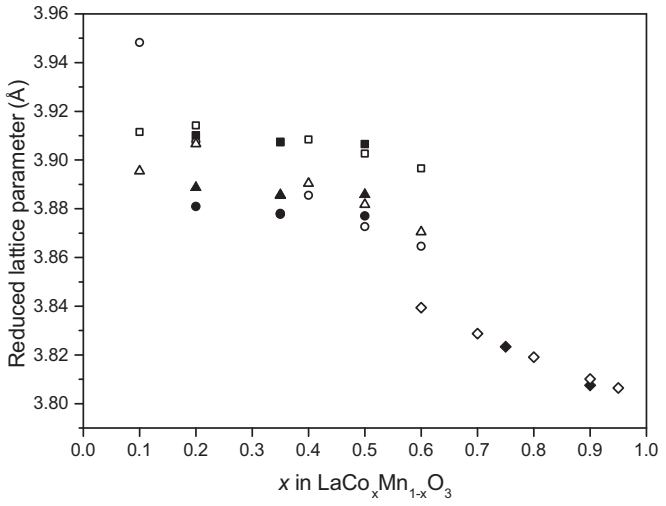

FIG. 5. Determined lattice parameters as a function of composition for the series $LaCo_xMn_{1-x}O_3$ for the orthorhombic and rhombohedral unit cells. Shown are the three equivalent lattice parameters (a_{pc}) for the cubic ABX_3 perovskite (where, for the orthorhombic lattice parameters, $a = \sqrt{2}a_{pc}$, $b = 2b_{pc}$, and $c = 2c_{pc}$ and for the rhombohedral unit cell $a = \sqrt{2}a_{pc}$). In this figure, values for a_{pc}, b_{pc}, and c_{pc} for the orthorhombic cells are shown as solid squares, triangles, and circles, respectively, and a_{pc} for the rhombohedral cells are shown as solid diamonds. The open symbols are the reported values from Autret *et al.* [10].

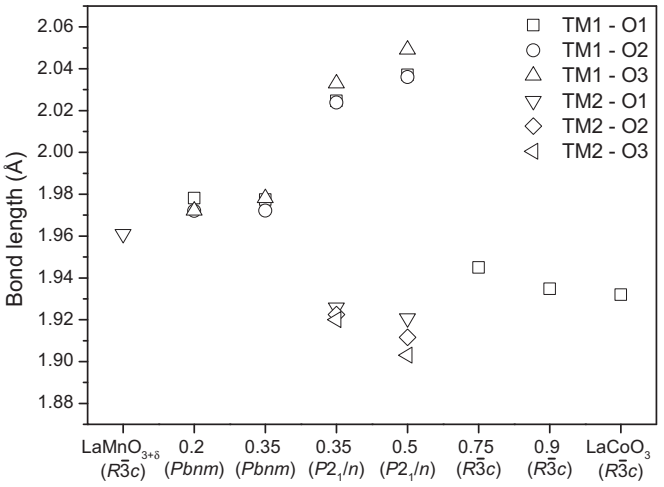

FIG. 6. Bond lengths obtained from Rietveld refinements for each member of the $LaCo_xMn_{1-x}O_3$ series. For the rhombohedral ($R\bar{3}c$) and orthorhombic ($Pbnm$) structures, only an average Co/Mn-O distance is determined as a result of site disorder. However, for the monoclinic $P2_1/n$ structure distinct Co-O (~2.02 Å) and Mn-O (~1.92 Å) bond distances are determined as the transition-metal ions Co and Mn are shown to be ordered and preferentially sited on the $2c$ and $2d$ Wyckoff sites, respectively (see Table II).

mixture of $LaCo_{0.85}Mn_{0.15}O_3$ and $LaCoO_{2.95}$. The structural parameters of each phase were refined and are shown in Table III. Taking into account the phase fractions of both phases, the total ratio of Co:Mn in the sample remains 0.9:0.1,

TABLE III. Structural parameters for the two phases found for the $x = 0.9$ sample. Overall goodness-of-fit parameters are $wR_p = 4.33\%$, $R_p = 2.45\%$.

		Phase 1	Phase 2
	Weight fraction	0.504(13)	0.496(13)
	Space group	$R\bar{3}c$	$R\bar{3}c$
	$a = b = c$ (Å)	5.3950(4)	5.38401(9)
	$\alpha = \beta = \gamma$ (°)	60.801(2)	60.792(1)
La	Wyckoff site	$2a$	$2a$
	x	0.25	0.25
	y	0.25	0.25
	z	0.25	0.25
	U_{iso} (Å^2)	0.003	0.0017(7)
	S.O.F.	1	1
Co/Mn	Wyckoff site	$2b$	$2b$
	x	0	0
	y	0	0
	z	0	0
	U_{iso} (Å^2)	0.002(5)	0.005(2)
	S.O.F. (Co)	0.85(1)	1
O1	Wyckoff site	$6e$	$6e$
	x	−0.1988(3)	−0.2010(3)
	y	0.6988(3)	0.7010(3)
	z	0.25	0.25
	U_{iso} (Å^2)	0.0015(7)	0.0053(7)
	S.O.F.	1	0.98(1)

as intended. Since this phase separation is observable only by high-resolution diffraction, we suggest that the limit of the $LaCo_xMn_{1-x}O_3$ solid solution is reached at $x = 0.85$.

2. Low temperature

Low-temperature neutron diffraction data were also obtained for each of the samples on the medium-resolution Polaris diffractometer. Datasets were obtained at 50 K (significantly below the magnetic ordering temperature) with a view to obtaining details of the magnetic structure.

For the compositions $x = 0.2, 0.35$, and 0.5, enhanced intensity of the 110/002 and 112/020/200 reflections is consistent with ferromagnetic ordering along the c-axis, magnetic space group $Pb'n'm$, similar to our previous report [25]. The refined ordered moments are reported in Table I. We stress that due to limitations of data quality and instrument resolution, we used the orthorhombic symmetry to model the magnetic structure of all three samples, despite the nuclear structures of the $x = 0.35$ and 0.5 samples being better described by the monoclinic structure. The magnetic structure of $LaCo_{0.5}Mn_{0.5}O_3$ was recently explored by Orayech *et al.* [22], who identified three potential, though indistinguishable, ferromagnetic models in space groups $P2_1/n$ and $P2_1'/n'$.

In contrast, for the $x = 0.75$ and 0.9 samples, no extra reflections are observed, even on cooling to 4 K. The lack of reflections with magnetic origin suggests that there is no long-range magnetic ordering in the materials at this temperature. This is consistent with the observation of only a weak ferromagnetic signal in the dc susceptibility. However, we do note that if $k = 0$, the additional intensity will be on the nuclear peaks and hence if small, masked by atomic displacement parameters. Despite being statistically acceptable, careful visual inspection of these fits revealed some discrepancies in peak shape and position that could not be resolved using the medium-resolution data. Hence, a high-resolution study was carried out on the HRPD instrument. We note briefly that for $x = 0.9$, the two-phase mixture described above for the room-temperature data also produced a satisfactory fit to the 4-K data. In contrast, the high-resolution neutron diffraction study of the sample with composition $x = 0.75$ at low temperature shows some interesting features. There are significant shoulders to the reflections which are particularly observable around 2.25 Å. We have made significant effort to fit this data set with the rhombohedral structure in combination with other possible oxides containing La,Co, and Mn, including the parent perovskites of the series. None of these materials were able to satisfactorily fit the diffraction pattern. To this end we tried a lower-symmetry crystalline structure for the majority perovskite phase. This was achieved initially by reducing the symmetry to triclinic $P\bar{1}$, with $a = 5.393\,02(28)$ Å, $b = 5.378\,40(58)$ Å, $c = 5.393\,03(28)$ Å, $\alpha = 61.003(3)^\circ$, $\beta = 61.003(5)^\circ$, and $\gamma = 61.003(3)^\circ$. We note this metric has $a = c \neq b, \alpha \sim \beta \sim \gamma$. Upon conversion to a more standard monoclinic perovskite space group, $I2/a$, the lattice parameters refine as $a = 7.670(7)$ Å, $b = 5.472\,9(5)$ Å, $c = 5.382\,1(5)$ Å, and $\beta = 91.082(4)^\circ$. The quality of fit by Rietveld refinement was given as $wR_p = 3.62\%$ (which should be compared with the value of 4.64% that was obtained using the rhombohedral setting). While not fully satisfactory, the fit did improve, as evidenced by the splitting of the 210 reflection from $R\bar{3}c$ at ~2.31 Å to $11\bar{2}$, 310, and 121 at ~2.31 Å and $12\bar{1}$ at ~2.33 Å in $I2/a$ (Fig. 7). In this model the Co and Mn are disordered on the 4b Wyckoff site, with TM–O bond lengths ranging from 1.855 Å to 2.016 Å, entirely consistent with Mn–O and Co–O bond lengths of varying TM oxidation states. We suggest that this complicated monoclinic structure could be used as a starting point for future studies of this material and may start to account for the unusual magnetic behavior of the materials in this series with high cobalt content.

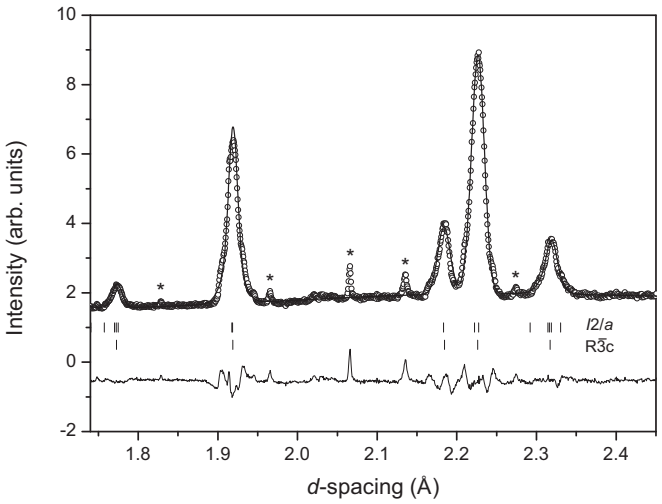

FIG. 7. Selected region of the Rietveld refinement of the monoclinic ($I2/a$) model for $LaCo_{0.75}Mn_{0.25}O_3$ using high-resolution neutron data obtained from HRPD. Also shown are the allowed reflections for the rhombohedral ($R\bar{3}c$) structure, which highlights the improvement in fit obtained by reducing the symmetry of the model. The reflections marked with asterisks are attributed to the cryostat background.

The complete lack of magnetic Bragg reflections combined with the weakly ferromagnetic nature of the $x = 0.75$ sample prompted a detailed investigation of this material using ac susceptibility. The real part of the ac susceptibility, χ', as shown in Fig. 8(a), has a peak at ~218 K and a broad maxima at ~25 K. The imaginary part of the ac susceptibility, χ'', is nonzero at temperatures lower than about 235 K, again contains a peak at 218 K, and the broad maxima at low temperature has sharpened into a second peak. The 218 K feature does not exhibit a frequency dependence (see the upper panel of Fig. 9), which implies that it arises from a ferromagnetic ordering transition. Given the lack of magnetic Bragg peaks, it is clear that the coherence length of this ordering is rather small. Conversely, the position of peak at ~25 K does exhibit a clear frequency dependence across the range measured (250–10 000 Hz). Such a dependence, observed at the relatively low frequencies used here, is indicative of some form of frustrated and/or glassy ordering [32]. The magnitude of the frequency dependence can be approximated by the relationship $\Delta T_f/T_f\Delta(\log\omega)$, as per Mydosh [32]. Values for T_f at each frequency were obtained by fitting a quadratic function of the form $\chi'' = A + B(T - T_f)^2$ to the peaks in the temperature dependence of χ'', and a value of 0.094 was obtained for the Mydosh parameter. This value

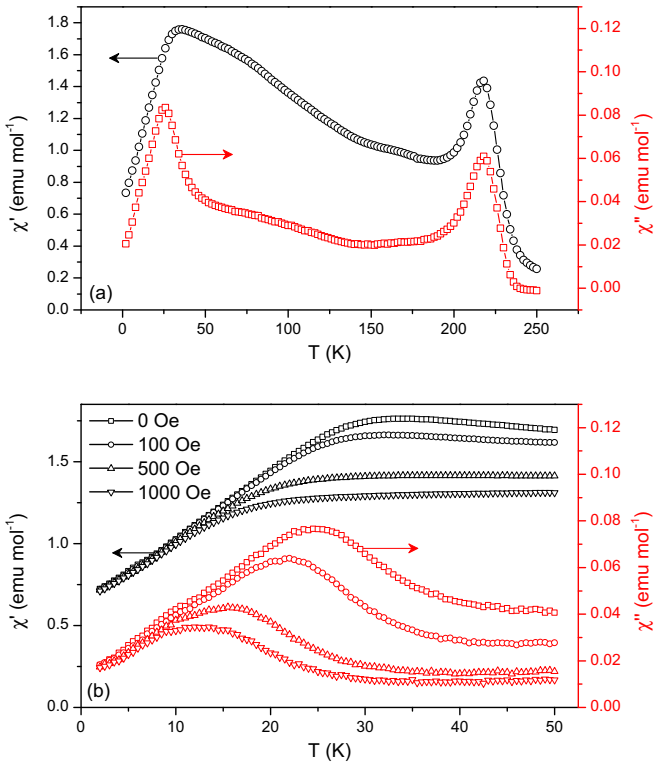

FIG. 8. (a) Real and imaginary parts of the ac susceptibility of $LaCo_{0.75}Mn_{0.25}O_3$ as a function of temperature (2–250 K), measured at 1.016 kHz with 0 dc bias field. (b) The 0–50 K region of the ac susceptibility measured at 255 Hz in various dc bias fields.

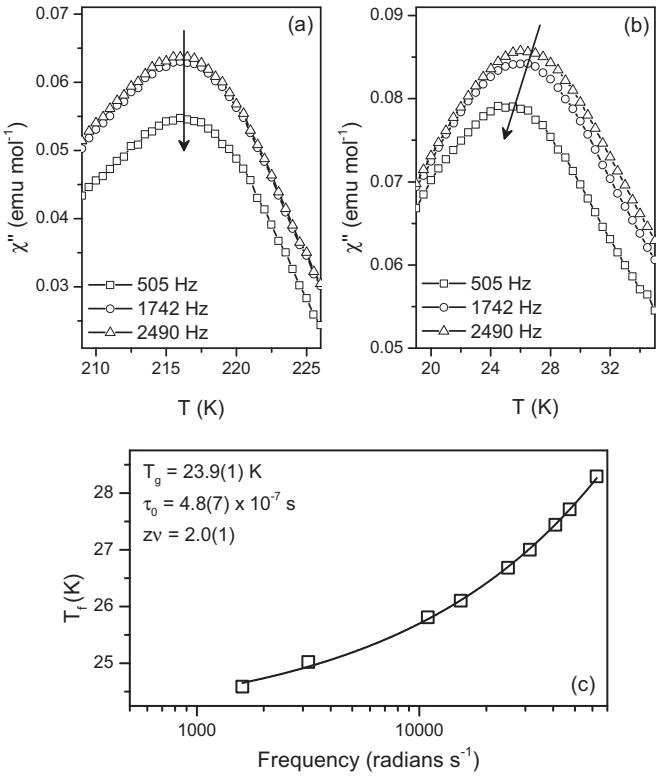

FIG. 9. (a, b) Close-up views of the two peaks in the imaginary part of the ac susceptibility of $LaCo_{0.75}Mn_{0.25}O_3$ at three different frequencies. The frequency dependence in the position of the ∼25 K peak is clear. Arrows are a guide to the eye. (c) Result of fitting the frequency dependence of T_f with the conventional critical "slowing down" model.

is larger than those observed for canonical spin glasses (which tend to lie in the range 5×10^{-3}–2×10^{-2}) and significantly smaller than those expected for superparamagnets ($\gg 0.1$) [32]. Some specific examples include 0.013 for double-perovskite $SrLaCoReO_6$ [33], 0.022 for Sr_2FeTeO_6 [34], and 0.085 for $LaCo_{0.5}Mn_{0.5}O_3$ [35]. Intermediate values of the Mydosh parameter are commonly observed in so-called cluster glasses where weakly interacting ferromagnetic clusters are randomly oriented [36–38]. The magnitude of the frequency dependence, in general, can be related to the strength of interaction between the magnetic entities [37,39]. In the case of an ordered ferromagnetic system, this interaction (between atoms) is strong and hence very high frequencies (well outside the range explored here) are required to see any frequency dependence. Conversely, an idealized superparamagnetic system consisting of noninteracting particles (for example, α-$Ho_2O_3(B_2O_3)$ [32]) has a much higher sensitivity to frequency and thus a larger value of the Mydosh parameter. To further characterize the dynamics of the magnetic behavior of this material, the low-temperature peak in the ac susceptibility was probed at several additional frequencies, and an attempt was made to fit the frequency dependence of T_f to the Vogel-Fulcher law, but the fitted parameters were unphysical. Therefore the data were fitted using the Ogielski scaling relation [40,41], $T_f = T_g[1 + (f\tau_0)^{1/z\nu}]$, where T_g is the "phase transition" temperature, equivalent to extrapolating T_f to 0 Hz, τ_0 is a characteristic time of the system, and $z\nu$ a critical exponent. The fit is shown in Fig. 9 and the values obtained were $T_g = 23.9(1)$ K, $\tau_0 = 4.8(7) \times 10^{-7}$ s, and $z\nu = 2.0(1)$. The characteristic time is indicative of rather slow spin-flipping dynamics and indeed is rather higher than those typically obtained for canonical spin glasses, but well within the range reported for reentrant spin glasses and cluster glasses such as Nd_5Ge_3 (10^{-7} s) [42], $La_{0.95}Sr_{0.05}CoO_3$ (10^{-10} s) [43], $LaCo_{0.5}Ni_{0.5}O_3$ (10^{-5} s) [44], and $LaMn_{0.5}Fe_{0.5}O_3$ (10^{-5} s) [45]. The evidence from ac susceptibility overwhelmingly suggests that the behavior of $LaCo_{0.75}Mn_{0.25}O_3$ can be classified as a cluster glass. This behavior is very similar to the reentrant spin-glass behavior observed in $LaCo_{0.5}Ni_{0.5}O_3$ [44], and the "glassy ferromagnetism" reported several times for $La_{1-x}Sr_xCoO_3$ [46,47].

E. Phase diagram

In Fig. 10 we present the structural and magnetic phase diagram of the solid solution $LaCo_xMn_{1-x}O_3$. For each of the materials the synthetic conditions were identical. At room temperature, a composition-dependent transition from orthorhombic to monoclinic and then rhombohedral is observed. The monoclinic symmetry, as reported previously for $x = 0.5$ [14] and here for $x = 0.35$, is a result of transition-metal cation ordering. Also shown is the orthorhombic/monoclinic-to-rhombohedral boundary and regions of phase coexistence. The regions of phase coexistence are quite large as a result of

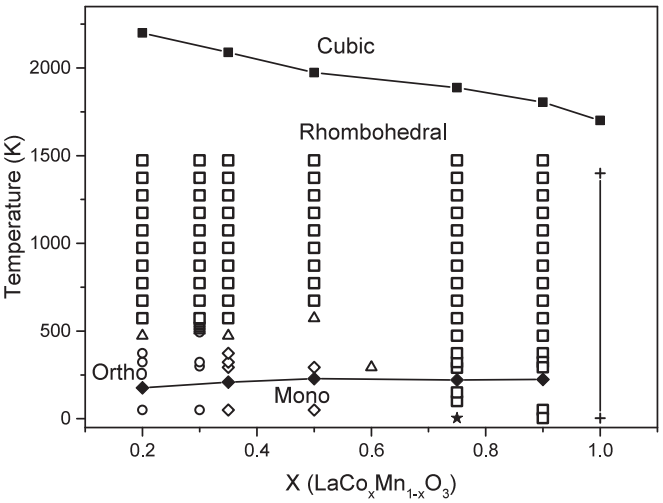

FIG. 10. Phase diagram of the $LaCo_xMn_{1-x}O_3$ series as a function of temperature. The points where the orthorhombic symmetry materials exist are shown as open circles (○). Regions where rhombohedral symmetry exist are shown by open squares (□). Regions of phase coexistence (both orthorhombic/monoclinic and rhombohedral symmetry) shown as open triangles (△). Monoclinic regions are shown by open diamond (◊). The extrapolated transition temperature from rhombohedral to pseudocubic symmetry is shown by the joined solid squares (■). The rhombohedral phase of $LaCoO_3$ has been shown to exist from 4 to 1400 K by Thornton *et al.* [7] and is shown by the crosses (+); data is also shown for the $x = 0.33$ sample from previous work [25]. The Curie temperature for each ferromagnetic transition is also shown as a solid diamond (⧫). Finally, the proposed monoclinic phase is shown as a solid star for the sample with the composition $x = 0.75$.

the strain inherent in these samples (as indicated by the peak width in the diffraction patterns, especially noticeable if you compare that to the parent materials synthesized by the same routes). The extrapolated second-order phase transition to the metrically cubic phase is also shown, this transition being well below the melting points for the parent compounds, 2013 K and 2153 K for $LaCoO_3$ and $LaMnO_3$, respectively [48,49]. Also shown are the ferromagnetic ordering temperatures for each material studied as described in Sec. III D and in tabulated in Table I.

IV. CONCLUSIONS

We have investigated the structural and magnetic phase diagram of the solid solution $LaCo_xMn_{1-x}O_3$ using x-ray and neutron diffraction and magnetometry techniques. We have shown that for the composition $x = 0.35$ the transition metals are site ordered and the sample crystallizes with a monoclinic crystallographic structure $P2_1/n$. We have also confirmed the disordered nature of the transition-metal ions in the compositions $x = 0.2$, 0.75, and 0.9. Phase separation is observed in high-resolution neutron diffraction for $x = 0.9$ and suggests that the solid solution limit is in fact $x = 0.85$. Structurally, we have also presented evidence to suggest that the rhombohedral $x = 0.75$ composition at low temperature transforms into a monoclinic structure.

We have also been able to map out a potential phase diagram as a function of temperature and have shown that there are a series of temperature-driven transitions from orthorhombic/monoclinic to rhombohedral and then to cubic. Transition temperatures are composition dependent. Further evidence is provided (by neutron diffraction and ac and dc magnetometry methods) that the nature of the low-temperature magnetic structure in the rhombohedral phases ($x = 0.75$ and 0.9) is glassy in nature. The ferromagnetic nature of the orthorhombic and monoclinic materials has also been confirmed by use of neutron diffraction.

ACKNOWLEDGMENTS

The authors acknowledge access to the ISIS neutron facility at Science & Technology Facilities Council (STFC) and Materials Characterization Laboratory capabilities therein. We also acknowledge the cryogenic technical support given by Dave Bunce of ISIS. Finally, we are grateful to Alexandra Gibbs for useful discussions.

[1] A. P. Ramirez, J. Phys.: Condens. Matter **9**, 8171 (1997).
[2] H. Zhu, P. Zhang, and S. Dai, ACS Catal. **5**, 6370 (2015).
[3] J. Hu, L. Wang, L. Shi, and H. Huang, Electrochim. Acta **161**, 115 (2015).
[4] X. Ge, B. Li, D. Wuu, A. Sumboja, T. An, T. S. A. Hor, Y. Zong, and Z. Liu, J. Mol. Eng. Mater. **03**, 1540006 (2015).
[5] H. Liang, Y. Hong, C. Zhu, S. Li, Y. Chen, Z. Liu, and D. Ye, Catal. Today **201**, 98 (2013).
[6] K. Knížek, Z. Jiraák, J. Hejtmaánek, P. Henry, and G. André, J. Appl. Phys. **103**, 07B703 (2008).
[7] G. Thornton, B. C. Tofield, and A. W. Hewat, J. Solid State Chem. **61**, 301 (1986).
[8] A. M. Glazer, Acta Crystallogr., Sect. B: Struct. Crystallogr. Cryst. Chem. **28**, 3384 (1972).
[9] J. Rodriguez-Carvajal, M. Hennion, F. Moussa, A. H. Moudden, L. Pinsard, and A. Revcolevschi, Phys. Rev. B **57**, R3189 (1998).
[10] C. Autret, J. Hejtmánek, K. Knížek, M. Maryško, Z. Jirák, M. Dlouhá, and S. Vratislav, J. Phys.: Condens. Matter **17**, 1601 (2005).
[11] P. Ganguly, N. Y. Vasanthacharya, C. N. R. Rao, and P. P. Edwards, J. Solid State Chem. **54**, 400 (1984).
[12] Y. Wu, Z. Yu, and S. Liu, J. Solid State Chem. **112**, 157 (1994).
[13] J. B. Goodenough, A. Wold, R. J. Arnott, and N. Menyuk, Phys. Rev. **124**, 373 (1961).
[14] C. L. Bull, D. Gleeson, and K. S. Knight, J. Phys.: Condens. Matter **15**, 4927 (2003).
[15] G. H. Jonker, J. Appl. Phys. **37**, 1424 (1966).
[16] I. O. Troyanchuk, L. S. Lobanovsky, D. D. Khalyavin, S. N. Pastushonok, and H. Szymczak, J. Magn. Magn. Mater. **210**, 63 (2000).
[17] M. Sikora, Cz. Kapusta, K. Knížek, Z. Jirák, C. Autret, M. Borowiec, C. J. Oates, V. Procházka, D. Rybicki, and D. Zajac, Phys. Rev. B **73**, 094426 (2006).

[18] M. Maryško, Z. Jirák, K. Knížek, and C. Autret-Lambert, J. Magn. Magn. Mater. **322**, 1392 (2010).
[19] R. I. Dass and J. B. Goodenough, Phys. Rev. B **67**, 014401 (2003).
[20] T. Burnus, Z. Hu, H. H. Hsieh, V. L. J. Joly, P. A. Joy, M. W. Haverkort, H. Wu, A. Tanaka, H.-J. Lin, C. T. Chen, and L. H. Tjeng, Phys. Rev. B **77**, 125124 (2008).
[21] P. A. Joy, Y. B. Khollam, and S. K. Date, Phys. Rev. B **62**, 8608 (2000).
[22] B. Orayech, I. Urcelay-Olabarria, G. A. López, O. Fabelo, A. Faik, and J. M. Igartua, Dalton Trans. **44**, 13867 (2015).
[23] X. L. Wang, M. James, J. Horvat, and S. X. Dou, Supercond. Sci. Technol. **15**, 427 (2002).
[24] J. Krishna Murthy and A. Venimadhav, J. Appl. Phys. **111**, 024102 (2012).
[25] C. L. Bull, H. Y. Playford, K. S. Knight, W. G. Marshall, G. B. G. Stenning, R. I. Smith, and Z. Hart, J. Phys.: Condens. Matter **27**, 165401 (2015).
[26] C. J. Howard and H. T. Stokes, Acta Crystallogr., Sect. B: Struct. Sci. **54**, 782 (1998).
[27] S. A. Hayward, F. D. Morrison, S. A. T. Redfern, E. K. H. Salje, J. F. Scott, K. S. Knight, S. Tarantino, A. M. Glazer, V. Shuvaeva, P. Daniel, M. Zhang, and M. A. Carpenter, Phys. Rev. B **72**, 054110 (2005).
[28] M. A. Carpenter, C. J. Howard, B. J. Kennedy, and K. S. Knight, Phys. Rev. B **72**, 024118 (2005).
[29] Y. Kobayashi, T. Mitsunaga, G. Fujinawa, T. Arii, M. Suetake, K. Asai, and J. Harada, J. Phys. Soc. Jpn. **69**, 3468 (2000).
[30] M. A. Korotin, S. Yu. Ezhov, I. V. Solovyev, V. I. Anisimov, D. I. Khomskii, and G. A. Sawatzky, Phys. Rev. B **54**, 5309 (1996).
[31] M. W. Haverkort, Z. Hu, J. C. Cezar, T. Burnus, H. Hartmann, M. Reuther, C. Zobel, T. Lorenz, A. Tanaka, N. B. Brookes, H. H. Hsieh, H.-J. Lin, C. T. Chen, and L. H. Tjeng, Phys. Rev. Lett. **97**, 176405 (2006).
[32] J. A. Mydosh, *Spin Glasses, An Experimental Introduction* (Taylor & Francis, London, 1993).
[33] C. M. Thompson, L. Chi, J. R. Hayes, A. M. Hallas, M. N. Wilson, T. J. S. Munsie, I. P. Swainson, A. P. Grosvenor, G. M. Luke, and J. E. Greedan, Dalton Trans. **44**, 10806 (2015).
[34] L. Ortega-San Martin, J. P. Chapman, L. Lezama, J. J. Saiz Garitaonandia, J. Sánchez Marcos, J. Rodríguez-Fernández, M. I. Arriortua, and T. Rojo, J. Mater. Chem. **16**, 66 (2006).
[35] J. Krishna Murthy and A. Venimadhav, J. Appl. Phys. **113**, 163906 (2013).
[36] V. K. Anand, D. T. Adroja, and A. D. Hillier, Phys. Rev. B **85**, 014418 (2012).
[37] T. Chakrabarty, A. V. Mahajan, and S. Kundu, J. Phys.: Condens. Matter **26**, 405601 (2014).
[38] A. Malinowski, V. L. Bezusyy, R. Minikayev, P. Dziawa, Y. Syryanyy, and M. Sawicki, Phys. Rev. B **84**, 024409 (2011).
[39] K. Binder and A. P. Young, Rev. Mod. Phys. **58**, 801 (1986).
[40] A. T. Ogielski, Phys. Rev. B **32**, 7384 (1985).
[41] P. J. Baker, T. Lancaster, S. J. Blundell, M. L. Brooks, W. Hayes, D. Prabhakaran, and F. L. Pratt, Phys. B (Amsterdam, Neth.) **374-375**, 47 (2006).
[42] B. Maji, K. G. Suresh, and A. K. Nigam, J. Phys.: Condens. Matter **23**, 506002 (2011).
[43] D. N. H. Nam, R. Mathieu, P. Nordblad, N. V. Khiem, and N. X. Phuc, Phys. Rev. B **62**, 8989 (2000).
[44] M. Viswanathan and P. S. A. Kumar, Phys. Rev. B **80**, 012410 (2009).
[45] K. De, M. Thakur, A. Manna, and S. Giri, J. Appl. Phys. **99**, 013908 (2006).
[46] J. Wu and C. Leighton, Phys. Rev. B **67**, 174408 (2003).
[47] R. Caciuffo, D. Rinaldi, G. Barucca, J. Mira, J. Rivas, M. A. Senaris-Rodriguez, P. G. Radaelli, D. Fiorani, and J. B. Goodenough, Phys. Rev. B **59**, 1068 (1999).
[48] B. Gilbu, H. Fjellvåg, and A. Kjekshus, Acta Chem. Scand. **48**, 37 (1994).
[49] N. Q. Minh and T. Takahashi, *Science and Technology of Ceramic Fuel Cells*, edited by N. Q. M. Takahashi (Elsevier Science Ltd., Oxford, 1995).